Journal of Modern Optics, 2013
Vol. 60, No. 17, 1458–1465, http://dx.doi.org/10.1080/09500340.2013.765067

High harmonic cutoff energy scaling and laser intensity measurement with a 1.8 μm laser source

A.D. Shiner[a], C. Trallero-Herrero[a,b], N. Kajumba[a,c,d], B.E. Schmidt[e], J.B. Bertrand[a], Kyung Taec Kim[a,f], H.-C. Bandulet[e], D. Comtois[e], J.-C. Kieffer[e], D.M. Rayner[a], P.B. Corkum[a], F. Légaré[e] and D.M. Villeneuve[a]*

[a]*Joint Attosecond Science Laboratory, National Research Council of Canada and University of Ottawa, 100 Sussex Drive, Ottawa, Ontario K1A 0R6, Canada;* [b]*J.R. Macdonald Lab, Physics Department, Kansas State University, Manhattan, KS 66506, USA;* [c]*Department für Physik der Ludwig-Maximilians-Universität, Schellingstrasse 4, D-80799 Munich, Germany;* [d]*Max-Planck-Institut für Quantenoptik, Hans-Kopfermann-Strasse 1, D-85748, Garching, Germany;* [e]*INRS-Énergie et Matériaux, 1650 boul. Lionel-Boulet, C.P. 1020, Varennes, Québec J3X 1S2, Canada;* [f]*Advanced Photonics Research Institute, Gwangju Institute of Science and Technology, 261 Cheomdan-gwagiro, Buk-gu, Gwangju 500-712, Korea*

(*Received 15 November 2012; final version received 5 January 2013*)

High harmonic generation in gas targets leads to the production of attosecond pulses. The process of high harmonic generation requires that the gas be ionized by an intense femtosecond laser field. The highest photon energy produced is related to the laser intensity times the wavelength squared. This cutoff is reached only if good phase matching is achieved. Using a laser with a wavelength of 1800 nm, we estimate the laser intensity in the gas jet by recording the ion yield, and simultaneously record the high harmonic spectrum. We show that the cutoff energy matches the measured intensity, confirming that good phase matching is achieved to 100 eV. We also use the ion collector to characterize the spatial size of the gas jet and to measure the confocal parameter of the laser beam, parameters that are useful for numerical modelling.

Keywords: high harmonic generation; phase matching

1. Introduction

In high harmonic generation (HHG), an intense ($> 10^{14}$ W cm^{-2}) femtosecond laser field ionizes an atom. The free electron is accelerated in the continuum by the laser field, and then recombines with the parent ion, leading to the emission of an extreme ultraviolet photon [1,2]. The acceleration of the electron in the field can be substantial, resulting in recollision energies of hundreds of electron volts and the production of soft x-ray photons [3–5]. This process is periodic, repeating every half-cycle of the laser field and this periodicity is observed in the spectrum as harmonics at odd multiples of the fundamental laser photon energy. The process is locked to the optical cycle of the driving laser, and the emission from all atoms in the focal volume adds coherently.

The maximum photon energy produced by high harmonic generation, called the cutoff, is given by classical arguments [1] as $\Omega_{\text{cutoff}} = 3.17U_{\text{p}} + I_{\text{p}}$, where the ponderomotive potential is defined as $U_{\text{p}} = E^2/(4\omega_0^2)$, and I_{p} is the ionization potential of the target atom or molecule, and ω_0 is the laser angular frequency. Here we use atomic units, such that $\hbar = e = m_e = 1$. The ponderomotive potential is proportional to the peak laser intensity I and the laser wavelength λ squared, $U_{\text{p}} \propto I\lambda^2$. To achieve a higher photon cutoff energy, one can increase either I or λ. The intensity can only be increased to the point that the entire gas sample is ionized, so it is advantageous to use longer wavelength laser sources [6]. Here we use a laser source with a wavelength of 1800 nm [7] and reach a cutoff of 100 eV.

In many experiments, the observed cutoff is less than the classical limit. This is thought to be caused by poor phase matching of the higher harmonics. The higher harmonics, having shorter wavelengths, are more sensitive to slight changes in the phase of the driving laser field [8], and this is expected to become even more significant for longer wavelength driving lasers. Therefore observation of emission near the predicted cutoff is an indication of good phase matching. Unfortunately it is experimentally difficult to accurately determine the peak laser intensity in the laser focus. One approach is to estimate the focal spot size based on the near-field laser beam size, but this tends to overestimate the intensity due to imperfections in the beam. Here we measure the actual

*Corresponding author. Email: david.villeneuve@nrc.ca

laser intensity in the same gas jet that generates the HHG by recording the number of ions produced. We then compare the cutoff law to the actual HHG spectra.

2. Experimental setup

Experiments were performed at the Advanced Laser Light Source (ALLS) at INRS-EMT using a Ti:Sapphire laser (Thales, 100 Hz, 80 mJ, 30 fs), which is described in [9,10]. The wavelength of the laser is shifted with an optical parametric amplifier (Light Conversion TOPAS-HE), broadened in a gas filled hollow fiber and then compressed with either chirped mirrors at 1.4 μm [11] or anomalous dispersion in fused silica glass at 1.8 μm [7]. The 7 mm diameter laser beam is focused with a 250 mm focal length spherical mirror, with an approximate f-number of 35. In the HHG source chamber, gas is emitted from a pulsed gas jet (Parker Series 9, 500 μm orifice) operating at a repetition rate of 50 Hz with a nominal backing pressure of 3 bar. With the jet operating, the source chamber pressure rises to a typical operating pressure of 10^{-4} torr. The laser is focused just below the jet orifice with an estimated gas density on the order of 10^{17} cm^{-3}.

The XUV emission propagates forward in the same direction as the laser beam and is collected by a XUV spectrometer composed of a 100 μm slit, a 1200 line per mm flat field grating, a microchannel plate detector and a CCD camera. Details of the experimental setup can be found in [9].

There are various geometries that are commonly used for the gas target in HHG experiments – tube [12], pulsed valve [13], gas cell [14,15] or capillary [5]. Pulsed valve gas sources are used in high harmonic spectroscopy applications [16,17] because the high pressure expansion produces rotationally cold molecules that can be aligned in space using impulsive alignment techniques [18,19]. Because the gas from such sources expands into the vacuum chamber, we have experimental access to the ions that are produced in the laser focus. We built a simple ion collector to measure the ions produced by the laser pulse. It was composed of a mesh 7 cm below the gas jet orifice, biased at –500 V and capacitively coupled to an oscilloscope to record the current pulse. Despite the high number of ions produced, we verified that its response was linear in the range of interest. Details of the ion collector are found in the Appendices.

3. Intensity calibration

In order to compare the HHG cutoff with the laser intensity, the laser intensity in the generating medium must be measured. This is more difficult than it sounds. One approach for intensity calibration is to measure the spot size of the laser at the focus and to estimate the intensity based on the pulse energy, spot size and pulse duration. In practice this approach is tedious and not very accurate as it is difficult to accurately measure the spot size, and to account for variations in mode quality. It is also tempting to use a velocity map imaging detector with circularly polarized laser light to accurately measure the laser intensity [20,21]. This approach has two shortcomings: it requires adding a quarter waveplate to the optics, and it must be performed in a second chamber so that it is not possible to record HHG spectra in parallel. In addition, it would be difficult to know exactly where in the gas jet each laser beam is focused. Therefore we employ an *in situ* intensity measurement that can take place in parallel with the HHG measurement.

We determine the laser intensity in the gas jet by measuring the relative number of ions produced, by placing an ion collector downstream of the gas jet. The details of the ion collector can found in the Appendices. Because the measured ion signal scales linearly with the number of ions in the laser focus (shown below), we can use the ion collector to measure the dependence of the ionization probability on pulse energy. We then apply a single-atom ionization rate model and integrate over the focal volume. The fitting procedure described below gives the proportionality factor that relates the laser pulse energy, which is easily measured outside the vacuum chamber, to the intensity in the interaction volume [22].

Accurate models are available for calculating the dependence of the field-ionization rate on laser intensity, for example the ADK model [23]. A more general version was developed by Yudin and Ivanov [24]. This non-adiabatic model has been extensively tested, and it has been shown that it gives comparable results to the ADK theory for intensities that are well described by the tunneling regime (with Keldysh parameter $\gamma \ll 1$) and remains accurate for intensities where there is a substantial multi-photon contribution to ionization ($\gamma > 1$). The validity of the Yudin–Ivanov model for $\gamma > 1$ has been verified experimentally in [25] in which comparisons with 3D TDSE results showed good agreement for $\gamma = 20$ and $\gamma = 1$ (see the supplementary information of [25]).

We employ a method based on [22]. This model is applicable if the gas region is small compared to the confocal parameter of the laser focus. We will show below that the gas jet has a thickness on the order of 0.5 mm, while the confocal parameter is 7 mm. The model assumes that the radial profile of the laser beam is Gaussian. The single-atom ionization rate is temporally integrated over the pulse duration, and spatially integrated over the radial distribution. Calculations for the mode-integrated ionization yield are shown as the solid (blue) curves in the semilogy plots in Figure 1. This type of plot has a characteristic shape given by an exponential

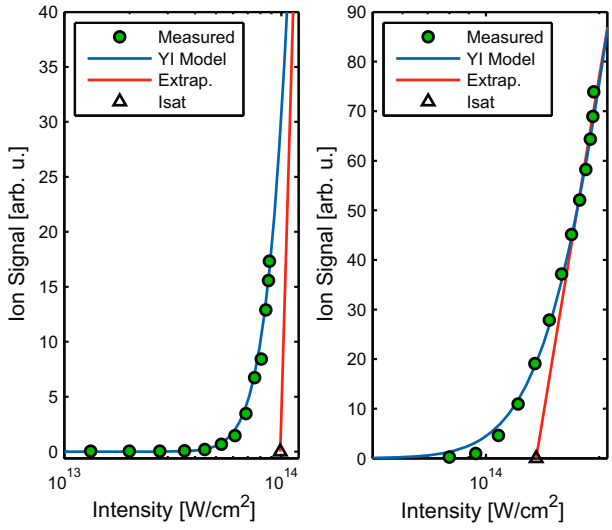

Figure 1. Measured intensity dependent ion signal in xenon (circles) fit to the mode integrated ionization yields calculated with the Yudin–Ivanov model (blue curves) for a 1.8 μm, 73 fs pulse (left) and a 1.8 μm, 11 fs pulse (right). If the sample is not strongly ionized (left), the peak intensity can be accurately determined by the fitting procedure. If the sample is strongly ionized (right) the asymptotic intensity dependence extrapolated to the intensity axis visually gives the saturation intensities (I_{sat}). The fitting procedure was used in all cases. (The color version of this figure is included in the online version of the journal.)

increase in the ionization yield as the intensity becomes high enough to ionize atoms in the most intense part of the focus. As the intensity increases the neutral atoms on axis are depleted and additional ions are produced on the wings of the Gaussian intensity distribution. The intensity dependence of the ionization rate once the on-axis atoms are fully ionized scales as the area of a disk. For our thin jet the intensity dependent ionization yield scales with the square of the spot size (area of a disk). We define the *saturation intensity* as the intensity at which 43% of the sample in the most intense, on axis, part of the focus is ionized. Extrapolating the asymptotic part of Figure 1 to the horizontal axis gives the saturation intensity [22]. Table 1 lists the calculated saturation intensities for a range of laser parameters and target atoms.

To find the proportionality factor that relates laser intensity to pulse energy, we measure the ion signal for a range of pulse energies. We then minimize the square error between theory and experiment by scaling the horizontal (intensity) axis of the measured data and the vertical (ionization yield) axis of the theoretical curve. This fitting procedure determines the absolute intensity of the laser in the interaction volume for a given pulse energy [22]. If the intensity is high enough to strongly saturate the sample, as was the case in the right panel of Figure 1, the proportionality factor can be estimated with a semilog plot of the ion signal with respect to pulse energy. Extrapolating the asymptotic part of the curve back to the horizontal axis gives the pulse energy that saturated the sample with the corresponding saturation intensity, I_{sat}, given in Table 1. The proportionality factor between the saturation intensity and energy can then be used to calculate the intensity for all other pulse energies. If the peak intensity was not high enough to strongly saturate the sample, such as in the left panel of Figure 1, the intensity axis can still be calibrated by using the fitting procedure described above. However, care should be taken to ensure that measurements come close enough to saturation in order to uniquely define the curve. In practice this can be checked by repeating the fitting procedure with a number of different initial seed values and ensuring that the fit always converges to the same value.

4. HHG cutoff

Since the ion collector does not interfere with the HHG measurement, it is possible to simultaneously record the ion yield and the HHG spectrum, and thereby relate the laser intensity to the HHG cutoff. In Figure 2 we show the HHG spectra that were recorded in parallel with

Table 1. Calculated saturation intensities for the noble gases using the Yudin–Ivanov nonadiabatic ionization model [24]. At the saturation intensity (I_{sat}), 43% of the sample on axis is ionized by the end of the pulse.

λ (nm)	Cycles	τ (fs)	$I_{sat}(10^{14}$ W cm$^{-2})$				
			Xe	Kr	Ar	Ne	He
800	2	5	1.60	2.85	4.51	14.4	23.0
800	10	27	1.01	1.81	2.86	9.10	14.5
800	20	53	0.86	1.54	2.44	7.75	12.3
1400	2	9	1.52	2.62	4.06	12.5	19.8
1400	10	47	1.03	1.77	2.72	8.28	13.0
1400	20	93	0.89	1.53	2.35	7.13	11.2
1800	2	12	1.45	2.47	3.81	11.6	18.4
1800	10	60	1.01	1.71	2.62	7.90	12.4
1800	20	120	0.88	1.49	2.27	6.82	10.7

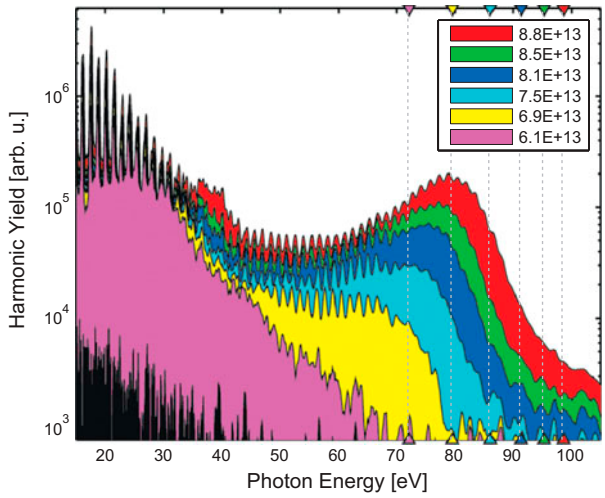

Figure 2. High harmonic spectra in xenon produced with a 1.82 μm, 73 fs pulse. The legend shows the intensity for each spectrum that was inferred using the ion collector (cf. Figure 1). The predicted cutoff energy for each spectrum, based on the inferred laser intensity I and using the relation $\Omega_{\text{cutoff}} = 3.17\ U_p + I_p$, is shown by the triangles on the horizontal axis. The predicted cutoff based on the measured intensity agrees within 3% of the observed HHG cutoff as determined by linearly extrapolating to the bottom of the graph, suggesting that high harmonic phase matching is excellent, despite the high degree of ionization. (The color version of this figure is included in the online version of the journal.)

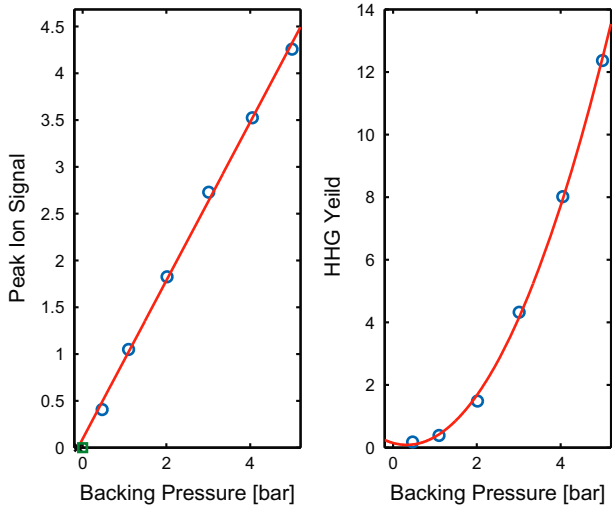

Figure 3. Measured ion signal from xenon as a function of pulsed valve backing pressure produced with a 1.3 μm, 130 fs pulse (left). The ion signal is proportional to the backing pressure, indicating that the ion collector signal is linear with the number of ions in the interaction volume. The harmonic yield (right) scales quadratically with backing pressure, indicating that the harmonic generation process was well phase matched. (The color version of this figure is included in the online version of the journal.)

the ionization measurements shown in the left panel of Figure 1. The peak around 80 eV is associated with the giant resonance in xenon, which we discuss elsewhere [26]. As the laser intensity increases, this peak becomes evident. The intensity calibration described above allows us to estimate the peak laser intensity for each spectrum, which is shown in the figure legend. Based on our calibration of the intensity, we plot in Figure 2 the expected cutoff $\Omega_{\text{cutoff}} = 3.17U_p + I_p$ for each spectrum with triangles and vertical lines. To define the cutoff energy, we extrapolate the linear part of each spectrum near the cutoff to the bottom of the graph. Since the curves are normalized to each other, this gives a fairly accurate measure of the cutoff frequency, although it is somewhat arbitrary.

The intensities inferred from these cutoffs agree to better then 3% with the intensities measured with the ionization method. This excellent agreement tells us that the HHG process for these conditions is almost perfectly phase matched over the entire spectrum. This highly phase matched process is surprising, considering that the highest intensity shown in Figure 2 (8.8×10^{13} W cm^{-2}) is very close to the saturation intensity of 9.74×10^{13} W cm^{-2} for the given laser conditions. At this intensity 29% of the atoms along the laser axis are ionized. Such a high degree of ionization is expected to cause plasma dispersion that will strongly affect the phase velocity of the 1.8 μm laser wavelength. Under these conditions we would expect poor phase matching. The fact that we observe excellent phase matching suggests that another mechanism is acting to compensate for the effect of plasma dispersion. The mechanism which permits the high cutoff despite strong ionization has been investigated in [27], and involves a spatial reshaping of the driving laser wavefront by the medium response. Further numerical modelling is called for, to fully understand the good phase matching.

5. Pressure scaling

A hallmark of phase-matched HHG is the coherent in-phase addition of the electric field of each emitting atom in the focal volume. If the phase velocity of the laser field is slightly different than that of the generated XUV, the front of the focal region will emit XUV that destructively interferes with that from the rear of the focal region. We showed in the previous section that the HHG cutoff increases according to the classical cutoff law. We now demonstrate that the emission scales quadratically with gas pressure.

The density of atoms under the jet scales linearly with jet backing pressure [28] so varying the pressure provides a convenient means of changing the number of ions produced in the focus. The results of this scan, in which the pressure was varied while the laser parameters were kept constant, are shown in Figure 3. In the left

panel, we observe a clear linear relation between ion signal and pressure. This verifies that the ion collector has a linear response in this region. The right panel of Figure 3 shows that the XUV photon yield increases quadratically with jet backing pressure. This demonstration of quadratic pressure scaling gives additional evidence of the good phase matching obtained with this laser source. Since we expect significant ionization of the gas, the number density of free electrons should increase linearly with gas pressure. It is not clear why the phase matching is not significantly affected by the gas pressure. Again, modelling of the propagation and phase matching is called for.

6. Summary and conclusions

We have demonstrated that we can accurately measure the peak laser intensity and relate it to the high harmonic cutoff frequency, using a femtosecond laser source with a wavelength of 1800 nm. By employing an ion collector below the pulsed gas jet, we are also able to characterize the density profile of the gas jet, and locate the gas jet relative to the laser beam waist (see Appendices). The latter two parameters are important when modelling the HHG process. We showed, with the present laser source, that the classical expression for the HHG cutoff frequency is in good agreement with the experimentally determined cutoff of the HHG spectrum. This implies that the phase matching of the HHG process at 1800 nm is much better than expected. Further modeling will be required to fully understand why the phase matching is so good.

Acknowledgements

We wish to thank Ray Pelletier for his assistance in fabricating the ion collector as well as Guy Lebrun for many useful discussions. We gratefully acknowledge funding from NSERC, AFOSR, CIPI and FQRNT.

References

[1] Corkum, P.B. *Phys. Rev. Lett.* **1993,** *71,* 1994–1997.
[2] Schafer, K.J.; Yang, B.; DiMauro, L.F.; Kulander, K.C. *Phys. Rev. Lett.* **1993,** *70,* 1599–1602.
[3] Shan, B.; Chang, Z. *Phys. Rev. A* **2001,** *65,* 011804.
[4] Takahashi, E.J.; Kanai, T.; Ishikawa, K.L.; Nabekawa, Y.; Midorikawa, K. *Phys. Rev. Lett.* **2008,** *101,* 253901.
[5] Chen, M.-C.; Arpin, P.; Popmintchev, T.; Gerrity, M.; Zhang, B.; Seaberg, M.; Popmintchev, D.; Murnane, M. M.; Kapteyn, H.C. *Phys. Rev. Lett.* **2010,** *105,* 173901.
[6] Popmintchev, T.; Chen, M.C.; Bahabad, A.; Gerrity, M.; Sidorenko, P.; Cohen, O.; Christov, I.P.; Murnane, M.M.; Kapteyn, H.C. *Proc. Natl. Acad. Sci. U.S.A.* **2009,** *106,* 10516–10521.
[7] Schmidt, B.E.; Béjot, P.; Giguère, M.; Shiner, A.D.; Trallero-Herrero, C.; Bisson, É.; Kasparian, J.; Wolf, J.; Villeneuve, D.M.; Kieffer, J.; Corkum, P.B.; Légaré, F. *Appl. Phys. Lett.* **2010,** *96,* 121109.
[8] Balcou, P.; Salières, P.; L'Huillier, A.; Lewenstein, M. *Phys. Rev. A* **1997,** *55,* 3204–3210.
[9] Shiner, A.D.; Trallero-Herrero, C.; Kajumba, N.; Bandulet, H.-C.; Comtois, D.; Légaré, F.; Giguère, M.; Kieffer, J.C.; Corkum, P.B.; Villeneuve, D.M. *Phys. Rev. Lett.* **2009,** *103,* 073902.
[10] Bandulet, H.C.; Comtois, D.; Shiner, A.D.; Trallero-Herrero, C.; Kajumba, N.; Ozaki, T.; Corkum, P.B.; Villeneuve, D.M.; Kieffer, J.C.; Légaré, F. *J. Phys. B: At., Mol. Opt. Phys*. **2008**, *41*, 245602.
[11] Giguère, M.; Schmidt, B.E.; Shiner, A.D.; Houle, M.A.; Bandulet, H.C.; Tempea, G.; Villeneuve, D.M.; Kieffer, J. C.; Légaré, F. *Opt. Lett.* **2009,** *34,* 1894–1896.
[12] Drescher, M.; Hentschel, M.; Kienberger, R.; Tempea, G.; Spielmann, C.; Reider, G.A.; Corkum, P.B.; Krausz, F. *Science* **2001,** *291,* 1923–1927.
[13] Salieres, P.; Ditmire, T.; Budil, K.S.; Perry, M.D.; L'Huillier, A. *J. Phys. B: At., Mol. Opt. Phys*. **1994**, *27*, L217.
[14] Tamaki, Y.; Itatani, J.; Nagata, Y.; Obara, M.; Midorikawa, K. *Phys. Rev. Lett.* **1999,** *82,* 1422–1425.
[15] Brichta, J.P.; Wong, M.C.H.; Bertrand, J.B.; Bandulet, H. C.; Rayner, D.M.; Bhardwaj, V.R. *Phys. Rev. A* **2009,** *79,* 033404.
[16] Wörner, H.J.; Bertrand, J.B.; Kartashov, D.V.; Corkum, P. B.; Villeneuve, D.M. *Nature* **2010,** *466,* 604–607.
[17] Wörner, H.J.; Bertrand, J.B.; Fabre, B.; Higuet, J.; Ruf, H.; Dubrouil, A.; Patchkovskii, S.; Spanner, M.; Mairesse, Y.; Blanchet, V.; Mével, E.; Constant, E.; Corkum, P.B.; Villeneuve, D.M. *Science* **2011,** *334,* 208–212.
[18] Rosca-Pruna, F.; Vrakking, M.J.J. *Phys. Rev. Lett.* **2001,** *87,* 153902.
[19] Stapelfeldt, H.; Seideman, T. *Rev. Mod. Phys.* **2003,** *75,* 543–557.
[20] Alnaser, A.S.; Tong, X.M.; Osipov, T.; Voss, S.; Maharjan, C.M.; Shan, B.; Chang, Z.; Cocke, C.L. *Phys. Rev. A* **2004,** *70,* 023413.
[21] Smeenk, C.; Salvail, J.Z.; Arissian, L.; Corkum, P.B.; Hebeisen, C.T.; Staudte, A. *Opt. Express* **2011,** *19,* 9336–9344.
[22] Hankin, S.M.; Villeneuve, D.M.; Corkum, P.B.; Rayner, D.M. *Phys. Rev. A* **2001,** *64,* 013405.
[23] Delone, N.B.; Krainov, V.P. *Usp. Fiz. Nauk.* **1998,** *41,* 469–485.
[24] Yudin, G.L.; Ivanov, M.Y. *Phys. Rev. A* **2001,** *64,* 013409.
[25] Uiberacker, M.; Uphues, T.; Schultze, M.; Verhoef, A.J.; Yakovlev, V.; Kling, M.F.; Rauschenberger, J.; Kabachnik, N.M.; Schroder, H.; Lezius, M.; Kompa, K.L.; Muller, H. G.; Vrakking, M.J.J.; Hendel, S.; Kleineberg, U.; Heinzmann, U.; Drescher, M.; Krausz, F. *Nature* **2007,** *446,* 627–632.
[26] Shiner, A.D.; Schmidt, B.; Trallero-Herrero, C.; Wörner; Patchkovskii, S.; Corkum, P.B.; Kieffer, J.C.; Légaré, F.; Villeneuve, D.M. *Nat. Phys.* **2011,** *7,* 464–467.
[27] Trallero-Herrero, C.; Jin, C.; Schmidt, B.E.; Shiner, A.D.; Kieffer, J.-C.; Corkum, P.B.; Villeneuve, D.M.; Lin, C.D.; Légaré, F.; Le, A.T. *J. Phys. B: At., Mol. Opt. Phys*. **2012**, *45*, 011001.
[28] Liepmann, H.W.; Roshko, A. *Elements of Gas Dynamics*; Wiley: New York, 1957.
[29] Salières, P.; L'Huillier, A.; Lewenstein, M. *Phys. Rev. Lett.* **1995,** *74,* 3776–3779.
[30] Balcou, P.; Salières, P.; L'Huillier, A.; Lewenstein, M. *Phys. Rev. A* **1998,** *55,* 3204–3210.

[31] Dudovich, N.; Smirnova, O.; Levesque, J.; Ivanov, M.; Yu; Villeneuve, D.M.; Corkum, P.B *Nat. Phys.* **2006,** *2,* 781–786.
[32] Kim, H.; Kim, I.; Tosa, V.; Kim, C.; Park, J.; Lee, Y.; Bartnik, A.; Fiedorowicz, H.; Nam, C.H. *IEEE J. Sel. Top. Quantum Electron.* **2004,** *10,* 1329–1338.
[33] Vozzi, C.; Negro, M.; Calegari, F.; Stagira, S.; Kovács, K.; Tosa, V. *New J. Phys.* **2011,** *13,* 073003.
[34] Verdeyen, J. *Laser Electronics*, 2nd ed.; Prentice-Hall: London, 1989.
[35] Gentry, W.R.; Giese, C.F. *Rev. Sci. Instrum.* **1978,** *49,* 595–600.

Appendix 1. Ion collector

The ion collector consists of a 102 mm diameter stainless steel mesh sandwiched between two fiberglass support rings and is positioned roughly 7 cm downstream from the gas jet. An illustration of the detector mounted below the pulsed jet is shown in Figure 4. The mesh is biased at –500 V through a 1 MΩ resistor and is coupled through a 2 nF capacitor to a high input impedance digitizing oscilloscope (Tektronix TDS-3054B).

The oscilloscope is triggered at the same time as the pulsed jet and is set to automatically acquire and average over a predefined number of laser shots (typically 32) before sending the averaged ionization trace to the computer. The response of the system is slower than the actual duration of the ion pulse, typically 150 μs. In the main text, we define 'ion yield' to be the peak value of the averaged trace. We also compared the peak value with the integrated trace, and found that both measures gave comparable scaling with intensity and pressure.

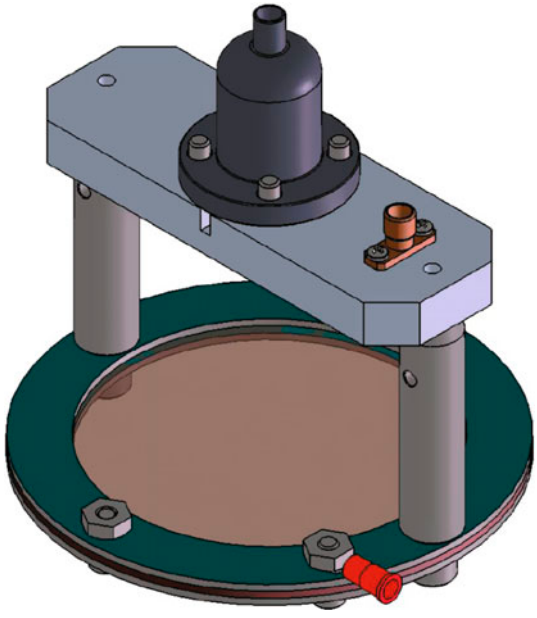

Figure 4. Illustration of the ion collector mounted below a Parker pulsed gas jet. The pulsed valve is the cylindrical structure at the top which emits pulses of gas in the downward direction. The ion collector is a simple wire mesh that is biased at –500 V. The mesh design permits the gas to pass through it without reflecting back to the pulsed valve. (The color version of this figure is included in the online version of the journal.)

Appendix 2. Gas jet position

In the main text of the paper, we demonstrated good agreement between the observed HHG cutoff and the prediction based on the measured laser intensity. We now go on to show that we can measure other parameters of the gas jet source. These parameters are important for optimizing the conditions for HHG. In addition, we are able to measure the density profile of the gas source as seen by the laser beam, and verify the confocal parameter of the laser beam; these parameters are needed to perform accurate modelling of the macroscopic HHG process. We can also absolutely locate the position of the gas jet relative to the laser beam waist.

High harmonic generation is a phase matched process and the position of the jet relative to the laser focus is a key parameter used to control phase matching [29]. It is generally known that placing the gas jet after the laser focus, where the pump beam is diverging, results in good phase matching for the short electron trajectories and poor phase matching for the long trajectories [30]. When the gas jet is moved towards the laser focus, the long trajectories become more collimated and can be measured separately from the short trajectories [31]. It is common for researchers working in this field to infer the relative jet position based on the divergence of HHG radiation. It was recently shown [10,32,33] that there are conditions where a low divergence XUV beam can be produced from focal positions where we would normally expect divergent *long trajectory* harmonics. Moving forward, it will be important to have a clear measurement of the position of the jet with respect to the focus.

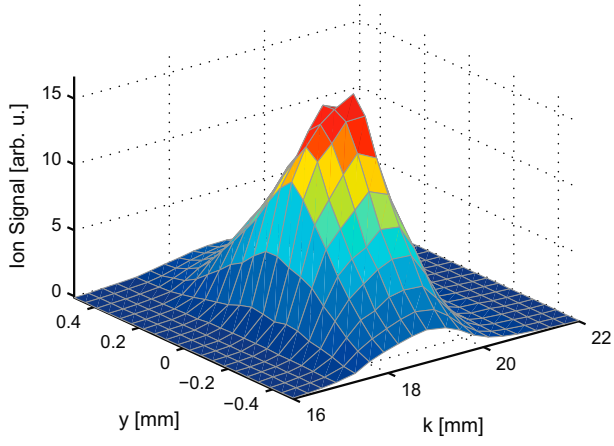

Figure 5. Ion signal as a function of jet position. The laser focus was held constant, while the gas jet was translated in two dimensions: parallel to the laser propagation direction, k, and perpendicular to both the laser propagation direction and the gas expansion direction y. Note that the laser conditions are different compared with other measurements reported in this paper. An 800 nm, 45 fs laser source was used, with a shorter confocal parameter. The gas jet conditions were 3 bar N_2, jet orifice $\phi = 500$ m. (The color version of this figure is included in the online version of the journal.)

While it is possible to estimate the jet position relative to the laser focus using a ruler when the vacuum chamber is open to air, we find that a far better approach is to scan the jet through the focus and locate the position where the ionization signal is maximized. This is not necessarily the same as the position at which the HHG signal maximizes. Figure 5 shows the dependence of ion signal on jet position. The position of the gas jet at which the ion signal peaks is where the laser beam waist is located directly under the gas jet. This method of locating the laser focus position is independent of the HHG process, since it only detects the amount of ionization. Therefore it is independent of any phase matching process.

Appendix 3. Focal parameters

Assuming Gaussian focusing, the laser spot size at the focus is defined by its $1/e$ field radius w_0 [34]. The beam diverges as we move away from the focus with the spot size $w(z)$ increasing as:

$$w(z)^2 = w_0^2\left[1 + \left(\frac{\lambda_0 z}{\pi w_0^2}\right)^2\right], \tag{1}$$

where λ_0 is the laser wavelength and z is the distance from the focus in the propagation direction. As the spot size increases, the on-axis intensity I_0 decreases as:

$$I_0(z) = I_0(z=0)\frac{w_0^2}{w(z)^2}. \tag{2}$$

By translating our thin jet along z, we measure an ionization signal that is characteristic of the beam divergence and intensity. Starting with a measurement of the laser intensity at the focus using the method described in Section 3, we use the Yudin–Ivanov model [24] integrated over the beam profile to calculate the z dependence of the ionization yield as a function of the beam waist w_0 at the focus. We then fit this result to the measured data and find the spot size that gives the best agreement. Figure 6 shows the result of this; we find satisfactory agreement for $w_0 = 64$ μm. Given the beam waist size w_0, the Rayleigh length z_0, which is defined as the distance from the focus where the spot size increases to $2^{1/2}\ w_0$, is:

$$z_0 = \frac{w_0^2}{\lambda_0}. \tag{3}$$

For our 1.8 μm laser with $w_0 = 64$ μm we find that $z_0 = 7.1$ mm. Examining Figure 6, we see that this distance corresponds to the position at which the ion yield decreases by about a factor of 2. Therefore we can accurately estimate the beam waist and the confocal parameter of the laser focus.

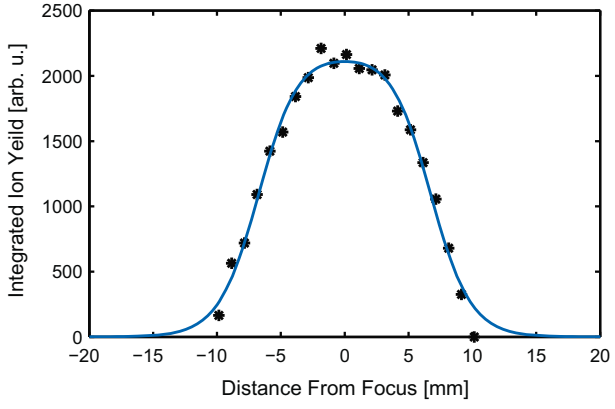

Figure 6. Measured dependence of ionization yield on jet position in the laser propagation direction (symbols). The solid curve shows the z dependence of the calculated mode integrated ionization yield for a thin sample in a laser field that is focused to a 64 μm spot. The corresponding confocal parameter is 7.1 mm. Conditions were 1.8 μm, 45 fs, $I(z = 0) = 2.44 \times 10^{14}$ W cm^{-2}, xenon. (The color version of this figure is included in the online version of the journal.)

Appendix 4. Gas jet density profile

The ion signal profile shown in Figure 5 reveals the density profile of the gas jet. The gas is emitted from the gas jet in a direction perpendicular to the orifice, a direction that we call the x-axis. The gas density profile will be cylindrically symmetric about the x-axis, $\rho(r,x)$, where r is the radial coordinate around x. We take the scan in the lateral direction y across the gas jet in Figure 5, at the position in the focal direction corresponding to the best focus. The experimentally measured ionization signal versus y can be Abel-inverted to give the actual radial density profile. Instead, we model the radial density profile as a Gaussian shape with

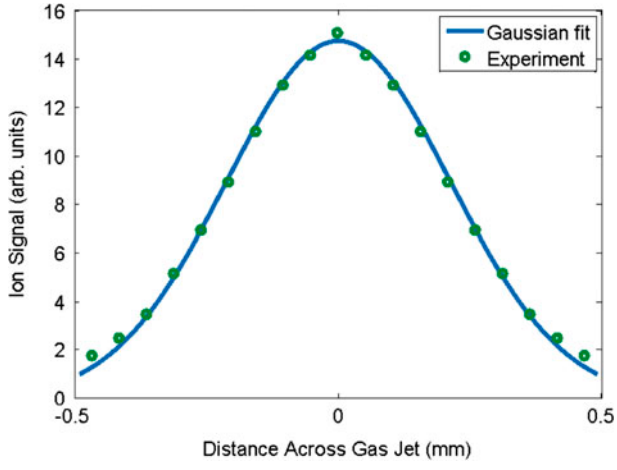

Figure 7. Measured lateral width of the pulsed valve gas jet density. The gas density is modeled as a Gaussian, $\rho(r) = \rho_0 \exp(-(r/r_0)^2)$. Line integrals through the model density profile are taken, yielding the solid line. The circles represent the measured ion signal as the gas jet is traversed across the laser beam at the position of best focus. The fitted $1/e$ half-width of density is 0.3 mm. (The color version of this figure is included in the online version of the journal.)

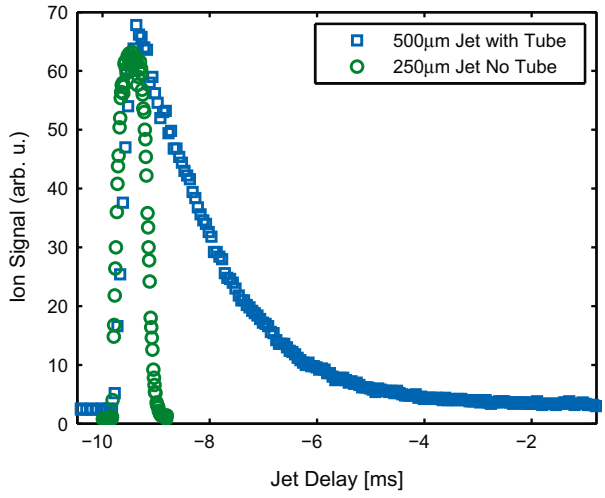

Figure 8. Ion signal as a function of the delay between the laser pulse and the gas jet trigger for two different jet configurations. The gas pulse from a 250 μm jet orifice expanding directly into the target chamber is shown as the green circles and the pulse from a 500 μm jet orifice with a small 14 mm long, 350 μm diameter tube mounted under the jet is shown in blue. The data is plotted so that the gas density at later times relative to the jet trigger signal are shown on the right side of the graph. Data were normalized so both curves have the same peak value. Conditions were 800 nm, 45 fs, 2–3 bar N_2 backing pressure. (The color version of this figure is included in the online version of the journal.)

width r_0, namely $\rho(r) = \rho_0 \exp(-(r/r_0)^2)$. We then integrate the predicted ionization signal along a line of constant y through the gas jet. The experimental signal is compared with the predicted signal, and the fitting parameters ρ_0 and r_0 are adjusted for the best fit, shown in Figure 7. The fit to the Gaussian profile is sufficiently good that it is not necessary to perform an Abel inversion. The inferred $1/e$ half-width of gas density is 0.3 mm, giving a FWHM of 0.5 mm.

The actual shape of the density profile of the gas jet is important when modeling the HHG process. In most cases the actual profile is not known. Here we show that the profile can be accurately measured. The actual Gaussian profile can be input into HHG propagation codes to predict the phase-matched HHG output.

Appendix 5. Pulsed jet timing

The ion detector described here has limited time resolution compared with time of flight mass spectrometers. The temporal resolution is hampered by the large number of ions that are produced in the gas jet, resulting in space charge effects that blur the mass resolution.

The timing of the pulse jet is chosen so that the laser interacts with the gas when the jet density is the highest. Ideally the jet will produce a gas pulse with very high density while the laser is present and turn off completely at all other times. In practice the ~ 1 ms gas pulses are dramatically longer than the <100 fs pulses produced by our lasers system. In order to measure the temporal profile of the gas pulses exiting a pulsed jet, dedicated instruments have been developed such as fast ionization detectors [35]. These are often used because the temporal profile of the gas pulse is an important diagnostic for correct operation of the jet. Here we show that we can directly measure the distribution of the gas pulse in time by varying the delay between the laser pulse and the electronic trigger for the pulsed jet controller. This is done with a delay generator (Stanford Research DG535) that is controlled with a GPIB interface. In Figure 8 we plot the measured gas pulse for two different jet configurations. First, we show the pulse from a $\phi = 250$ μm jet that expands directly into the target chamber, and then, we show the pulse from a $\phi = 500$ μm jet with a 14 mm long, $\phi = 350$ μm diameter tube mounted under the jet. The tube limits the flow of the gas and acts as a reservoir supplying gas for a few milliseconds after the jet solenoid has closed. We clearly see this behavior in the ion signal. Note that these datasets were recorded on different days and with slightly different laser conditions. They have been normalized to give the same peak ion signal.